Understanding helium transport: experimental and theoretical investigations of low-Z impurity transport at ASDEX Upgrade

A. Kappatou[1], R.M. McDermott[1], C. Angioni[1], P. Manas[1], T. Pütterich[1], R. Dux[1], E. Viezzer[2], R.J.E. Jaspers[3], R. Fischer[1], M.G. Dunne[1], M. Cavedon[1], M. Willensdorfer[1], G. Tardini[1] and the ASDEX Upgrade Team

[1] Max-Planck-Institut für Plasmaphysik, D-85748, Garching, Germany
[2] Department of Atomic, Molecular and Nuclear Physics, University of Seville, E-41012 Seville, Spain
[3] Science and Technology of Nuclear Fusion, Technische Universiteit Eindhoven, 5612 AZ, Eindhoven, The Netherlands

E-mail: athina.kappatou@ipp.mpg.de

Abstract. The presence of helium is fundamentally connected to the performance of a fusion reactor, as fusion-produced helium is expected to heat the plasma bulk, while He "ash" accumulation dilutes the fusion fuel. An understanding of helium transport via experimentally validated theoretical models of the low-Z impurity turbulent transport is indispensable to predict the helium density profile in future fusion devices. At ASDEX Upgrade, detailed, multi-species investigations of low-Z impurity transport have been undertaken in dedicated experiments, resulting in an extensive database of helium and boron density profiles over a wide range of parameters relevant for turbulent transport (normalised gradients of the electron density, the ion temperature, and the toroidal rotation profiles, the collisionality and the electron to ion temperature ratio). Helium is not found to accumulate in the parameter space investigated, as the shape of the helium density profile follows largely that of the electron density. Helium is observed to be as peaked as the electron density at high electron cyclotron resonance heating fraction, and less peaked than the electron density at high neutral beam heating fraction. The boron density profile is found to be consistently less peaked than the electron density profile. Detailed comparisons of the experimental density gradients of both impurities with quasilinear gyrokinetic simulations have shown that a qualitative agreement between experiment and theory cannot always be obtained, with strong discrepancies observed in some cases.

Manuscript
8 January 2019

1. Introduction

The shape of the helium density profile in future fusion reactors will have a serious effect on their performance, due to helium "ash" accumulation issues. Peaked helium concentration profiles cause dilution of the D-T fusion fuel in the plasma core, while hollow helium concentration profiles are preferable. To predict how the helium density profile will behave, understanding of the helium transport in fusion plasmas and experimental validation of the current theoretical understanding are required. In this paper, the helium density profiles measured in ASDEX Upgrade (AUG) are systematically compared to the available theoretical predictions to validate the theory and shed light on the behaviour of helium in future devices.

Previous investigations of helium transport at DIII-D showed that the helium density profile has a similar shape to the electron density [1]. At AUG, boron studies showed that the normalised logarithmic boron density gradients can be qualitatively, and even quantitatively, reproduced by gyrokinetic modelling if the "roto-diffusive" term, proportional to the normalised gradient of the toroidal rotation, is included [2, 3]. Moreover, previous gyrokinetic simulations of helium indicated that the thermodiffusive contribution to the particle flux should be more important for helium than for higher-Z impurities such as boron, leading to different peaking of the two species [4].

Therefore, dedicated experiments optimised for both helium and boron charge exchange measurements were performed at AUG. While carbon is also present in AUG, the concentration is too low to allow for studies with sufficient accuracy. The ability to fully interpret the helium charge exchange spectra [5] allows accurate helium density profiles to be derived and enables the inclusion of helium in these transport investigations. The aim of this undertaking is to determine the experimental correlation of the helium and boron density profile gradients with plasma parameters that are theoretically relevant to impurity transport, namely: the normalised gradients of the electron density, the electron and ion temperature, and the toroidal rotation profiles, as well as the electron to ion temperature ratio and the plasma collisionality. Furthermore, the comparison of the experimental observations with the predictions obtained from transport models puts the current theoretical understanding to the test. Systematic studies including multiple impurities, such as the one presented here, are necessary in order to have a deeper investigation of the transport physics of these species. Such multi-species studies allow a more stringent validation of the theoretical predictions and an assessment of the applicability of the present theoretical models of impurity transport to present and future fusion plasmas.

This study focusses on the confinement region (mid-radius). Light impurity transport has been observed to be dominated by anomalous transport in this region, with neoclassical transport being negligible [2, 3, 6], in the absence of internal transport barriers [7, 8]. The database collected for this study and the experimental observations are described in Section 2. In Section 3, the experimental data are compared to the theoretical predictions of the neoclassical transport and the transport due to the plasma turbulence. Detailed comparisons of the measured impurity density gradients with gyrokinetic simulations of the turbulent transport are presented. Conclusions are drawn

in Section 4.

2. Experimental investigation of helium and boron transport

2.1. Database of helium and boron density profiles

A database of helium and boron density profiles was assembled from a set of experiments performed at AUG, designed specifically for the investigation of helium transport and optimised for both helium and boron charge exchange measurements. The experiments were performed soon after a boronisation (coating of wall components produced by a glow discharge with 10% B_2D_6 and 90% He [9]), to ensure very good charge exchange signal from both impurities. Fresh boronisation also enables low density, low collisionality plasmas. It should be stressed that helium and boron are not puffed, but are rather "intrinsic" in the tokamak environment, due to the boronisation process.

The charge exchange measurements are performed on neutral beam injection source #3, one of the four sources of NBI box I, which has a maximum acceleration voltage of 60 keV. Two different spectroscopic instruments are used: the boron measurements were performed with the spectrometer described in [10] and the helium measurements were performed with the system described in [11]. Both measurements extend from the plasma center to approximately $\rho_{tor} = 0.85$. The helium density is measured at 15 or 24 plasma locations within this range (based on the diagnostic setup in each discharge), while the boron density is measured at 24 plasma locations. The radial resolution of the charge exchange measurements (not shown in the figure) is on the order of ± 1.5 cm, corresponding to a $\Delta\rho_{\rm tor} \sim 0.03 - 0.04$ at mid-radius. The NBI source used for the measurements was modulated and replaced by another injection source at the other side of the torus. This enables the subtraction of the passive emissions and reduces the uncertainties in the interpretation of the helium charge exchange spectra while keeping the total injected power constant.

All eleven discharges included in this database (#29083, #30367, #30368, #30374, #30379, #30380, #31432, #33399, #33400, #33401, #33431) were performed in a lower-single-null configuration, with a magnetic field of 2.5 T and a plasma current of 600 kA, with the exception of two discharges performed at higher plasma currents (800 kA and 1 MA). The applied electron cyclotron resonance heating (ECRH) power ranges from 0 – 4 MW and the neutral beam injection (NBI) power from 2.5 – 10 MW (at least one NBI source is needed for the CXRS measurements). The normalised confinement factor $H_{98(y,2)}$ for the cases selected is between 0.8 and 1.15.

The goal of these discharges was to provide boron and helium density profiles in scans of the experimental parameters expected to be relevant to the impurity transport in different turbulence regimes. The external actuators used in the experiment to influence the impurity density profiles are the NBI heating, the ECRH heating, and the plasma fuelling. These were varied to provide scans of the gradients of the electron density, the electron and ion temperature, and the toroidal plasma velocity profiles, as well as the electron to ion temperature ratio and the effective collisionality $\nu_{\rm eff}$, defined as the ratio of the electron-ion collision frequency to the curvature drift frequency. In the experiment,

all parameters change at once and it is not possible to keep certain parameters constant while changing others. However, by using different combinations of actuators, it is possible to separate the effect on the impurity profiles to some extent.

The application of central electron heating has been observed to have different effects on the electron density profiles under different conditions. A flattening of the electron density profile, also called "pump-out," has been observed in low density L-mode plasmas, but also at high densities, where it was partially attributed to the reduction of the Ware pinch [12, 13]. On the other hand, under certain conditions, the electron heating leads to peaking of the electron density profile [2, 13]. Through modelling of the turbulent transport, it has been shown that this behaviour can be explained by the turbulent plasma state. Adding electron cyclotron heating to an ion temperature gradient (ITG) turbulence dominated plasma, decreases the effective collisionality leading to a reduction of ITG and an increase of trapped electron mode (TEM) turbulence, which results in a peaking of the electron density profile. This is the case in low density, low current H-mode AUG plasmas, in which the electron density is observed to peak strongly with increasing central electron heating [2]. Furthermore, central deposition of ECRH leads to flat and even hollow rotation profiles, an effect connected to the plasma turbulence [14, 15]. A similar effect of the electron heating on light impurities was observed in AUG [2, 3]. This mechanism was used in the experiments described here to vary the peaking of the electron density, the plasma rotation, and the impurity density profiles, as well as the collisionality. Scans in NBI power were also performed to vary the Mach number and ion temperature, also using a combination of on- and off-axis beams in an attempt to vary the relatively stiff ion temperature profile, as well as the plasma rotation profile, by changing the torque and heat deposition profiles. Different levels of deuterium fuelling were also used to change the collisionality. Furthermore, discharges with different plasma currents were performed, to investigate the effect of the plasma magnetic equilibrium on the impurity profile gradients. The heating schemes of discharges #30367 and #30379 are shown in Fig. 1 as examples. In discharge #30367, a scan of ECRH power at constant NBI power was performed, in order to vary the peaking of the electron density profile. In discharge #30379, a scan of NBI power at constant ECRH power was performed, in order to see the effect of on- and off-axis beams [16] and NBI power levels on the impurity density profiles. Example averaged kinetic profiles for the time points indicated on the left are also shown.

A total of approximately 200 stationary phases, that were at least several tens of ms long were selected from these discharges to form the database analysed here. The term "stationary" corresponds to phases of the plasma discharges, during which the plasma parameters do not change significantly during multiple confinement times. The selected phases were restricted to time windows starting at least 40ms after the CXRS NBI source is switched on. The data points selected have been ELM-synchronised (only profiles before the crash were used) when ELMs were present, to avoid the strong effect of ELMs on the profiles. With the exception of discharge #29083, no strong sawteeth were documented in this database. When present, the sawteeth existed in the core, with an inversion radius inside $\rho_{tor} < 0.2$. Furthermore, no other strong MHD modes that could affect the transport were present.

An overview of the parameter space is given in Table 1 for $\rho_{tor} = 0.5$ (normalised

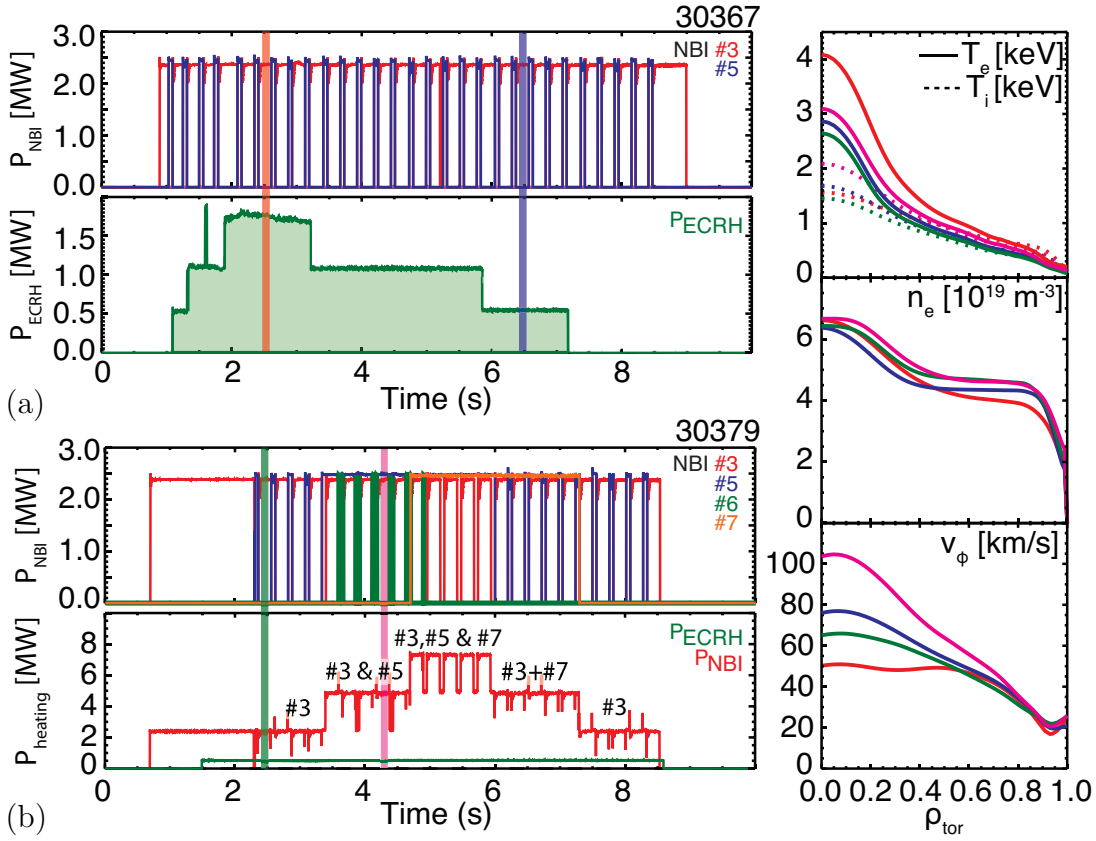

Figure 1. Heating schemes of two discharges from the helium transport database. a) In discharge #30367, a scan of ECRH power at constant NBI power was performed, in order to vary the peaking of the electron density profile. b) In discharge #30379, a scan of NBI power at constant ECRH power was performed, in order to see the effect of on- and off-axis beams and NBI power levels on the impurity density profiles. Example kinetic profiles for the time points indicated on the left are shown on the right.

toroidal flux coordinate, equal to 0 at the magnetic axis and 1 at the separatrix). The collisionality $\nu_{\rm eff}$ ($\sim 0.1\ n_e\ T_e^{-2}\ R\ Z_{\rm eff}$) at $\rho_{tor} = 0.5$ was varied by an order of magnitude, a factor of 3 in deuterium Mach number was achieved, and a large variation was also obtained in R/L_{n_e}, R/L_{T_i}, R/L_{T_e} and u' at mid-radius. These are the local normalised logarithmic gradients $\mathrm{R/L_X}$ defined as $-\frac{R}{X}\frac{\mathrm{d}X}{\mathrm{d}r}$ with r being the flux surface averaged plasma minor radius and R the plasma major radius, and the radial gradient of the toroidal plasma velocity given by $u' = -\frac{\mathrm{d}\Omega}{\mathrm{d}r}\frac{R^2}{v_{th}}$, where Ω is the angular toroidal rotation velocity. All plasma profiles are fitted with spline fits and the logarithmic gradients are calculated and averaged over $\rho_{\rm tor} = 0.45 - 0.55$.

The impurity density profiles were evaluated from the measured charge exchange intensities using the charge exchange impurity concentration analysis code CHICA [17]. The Monte Carlo simulation code FIDASIM [18, 19, 20] within CHICA was used for the neutral beam attenuation calculations, including the beam halo. The inclusion of the beam halo in the determination of the impurity density profiles is significant, as shown in [17]. Without it, the gradients of the calculated profiles can deviate significantly from the real ones ($\Delta R/L_{n_Z}$ of the order of ~ 1). The evaluation of the helium density profiles

Table 1. Parameter space covered in the helium transport database presented in this work. The values are given at $\rho_{tor} = 0.5$, with the exception of q_{95} (defined as the value of the safety factor q at the flux surface containing 95% of the total poloidal flux).

Parameter	Value range	Parameter	Value range
R/L_{n_e}	0.02 – 3.6	n_e	3.1 – 7.3·10^{19} m^{-3}
R/L_{T_e}	3.4 – 11.0	T_e	0.5 – 1.8 keV
R/L_{T_i}	3.0 – 8.7	T_i	0.5 – 1.6 keV
u′	-0.33 – 1.77	Mach	0.08 – 0.26
ν_{eff}	0.27 – 2.6	q_{95}	4.0 – 7.5 (∼7.1 at I_p=600 kA)

takes into account the plume "effect" [21], using a detailed forward model for the plume emission [5]. Electron density and temperature profiles derived from the Integrated Data Analysis scheme [22] and ion temperature and rotation profiles measured with charge exchange recombination spectroscopy on boron were used as inputs to the impurity concentration analysis code and to the plume modelling code. The plasma equilibrium is obtained from the high time resolution CLISTE code [23].

2.2. Experimental observations

Through the wide range of plasma parameters achieved in the experiments, a wide variety of experimental helium and boron density profiles were obtained, from strongly peaked to clearly hollow: A peaked profile is characterised by a higher impurity density level in the core than further out in the plasma, while a hollow profile is characterised by a lower value in the core than further out in the plasma. Local peaking or hollowness of the profiles can also be observed.

Example impurity density profiles from this database are shown in Fig. 2. These profiles were selected to illustrate the range of profile shapes that can be obtained. It also shows that the shapes of the helium and boron density profiles can be very similar (dashed lines), or very different (solid lines), depending on the background plasma parameters. As will be discussed in Sec. 3, differences in the profile shapes of impurities with different Z, or Z/A, are expected. The shown error bars correspond to the uncertainties on the intensity calibrations of the diagnostics (on the order of 10-15%) and the uncertainty on the calculation of the beam neutrals, which is required for the determination of the impurity densities. The uncertainty on the impurity density profiles can be up to 20%. The uncertainty on the electron density profile obtained by IDA is assumed to be on the order of 10% (though it can be much larger locally and depending on the quality of the input data). As a result, the uncertainty on the impurity density peaking defined as the ratio of the density values at two plasma locations is $\sim 30\%$ and the uncertainty on the electron density peaking $\sim 15\%$.

It is useful to compare the peaking of the impurity density profiles with the peaking of the electron density. If the impurity densities are more peaked than the electron density, the impurity is accumulating in the plasma core. Such an accumulation should be avoided in a future fusion reactor, as it would dilute the fusion fuel. In the following description of the experimental observations, the peaking of the helium, boron and electron density

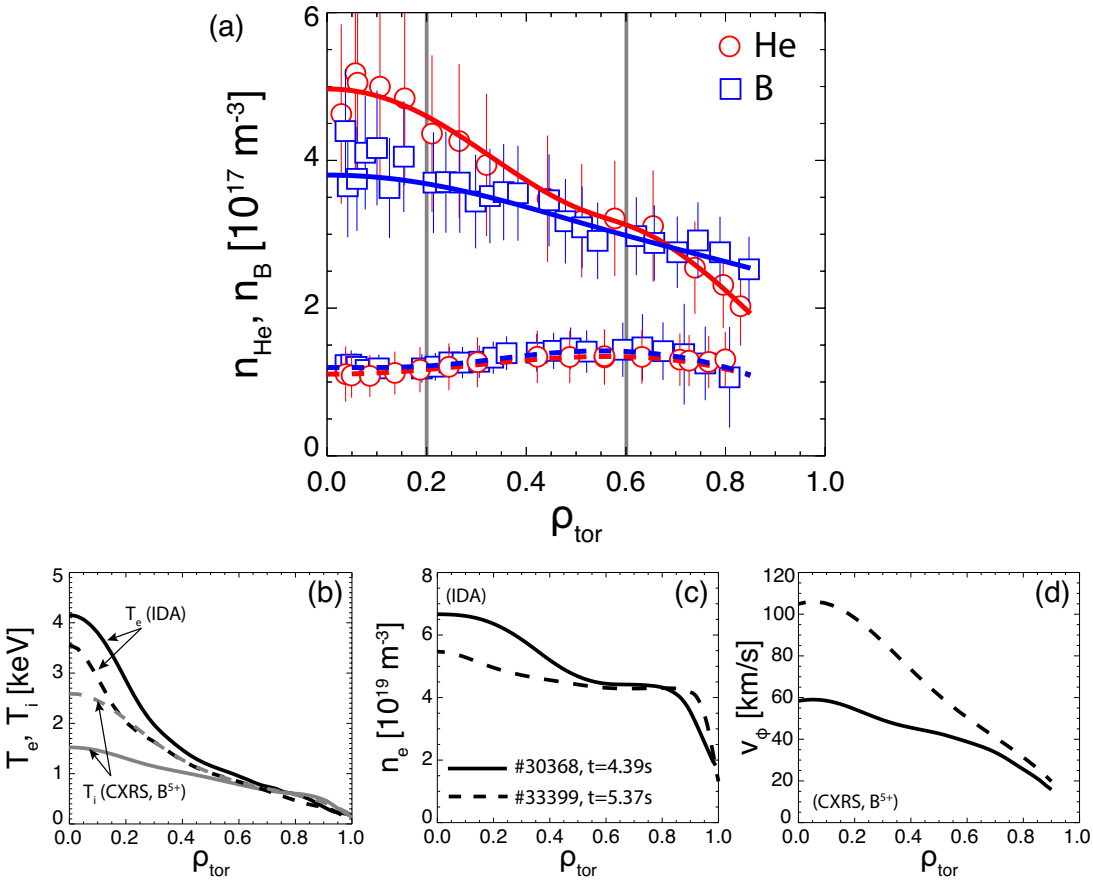

Figure 2. a) Example profiles of helium (red circles) and boron (blue squares) density profiles: two sets of profiles are shown, for #30368, t=4.39 s ($P_{NBI} = 2.4$ MW, $P_{ECRH} = 2.35$ MW, D-fuelling= $2.8 \cdot 10^{21}$ e/s) and for #33399, t=5.37 s ($P_{NBI} = 5.0$ MW, $P_{ECRH} = 1.4$ MW, D-fuelling= $3.7 \cdot 10^{21}$ e/s), with solid and dashed lines, respectively. The corresponding plasma kinetic profiles are shown in the lower plots: b) T_e and T_i, c) n_e and d) v_ϕ.

profiles, defined as $n_X(\rho_{tor} = 0.2)/n_X(\rho_{tor} = 0.6)$ with X being He (red circles), B (blue squares) or electrons (green triangles) is plotted. In Fig. 3, the peaking of the helium (left) and boron (right) is plotted versus the peaking of the electron density. Within the experimental uncertainties, indicated with the dashed lines, the helium density is as peaked as the electron density for the majority of the database, in agreement with previous investigations at DIII-D [1]. The boron density is consistently less peaked than the helium density. The points corresponding to the profiles shown in Fig. 2 are indicated with stars in Fig. 3.

As described in the previous section, the external actuators used in the experiment to influence the impurity density profiles are the NBI heating, the ECRH heating and the plasma fuelling. The effects of the heating power and deuterium fuelling scans on the impurity and electron density profiles are presented here. It should be stressed, however, that each actuator affects more than one plasma parameters simultaneously, which consequently makes the decoupling of the dependences not straightforward. The details of the observations should be considered on the basis of the local plasma parameters

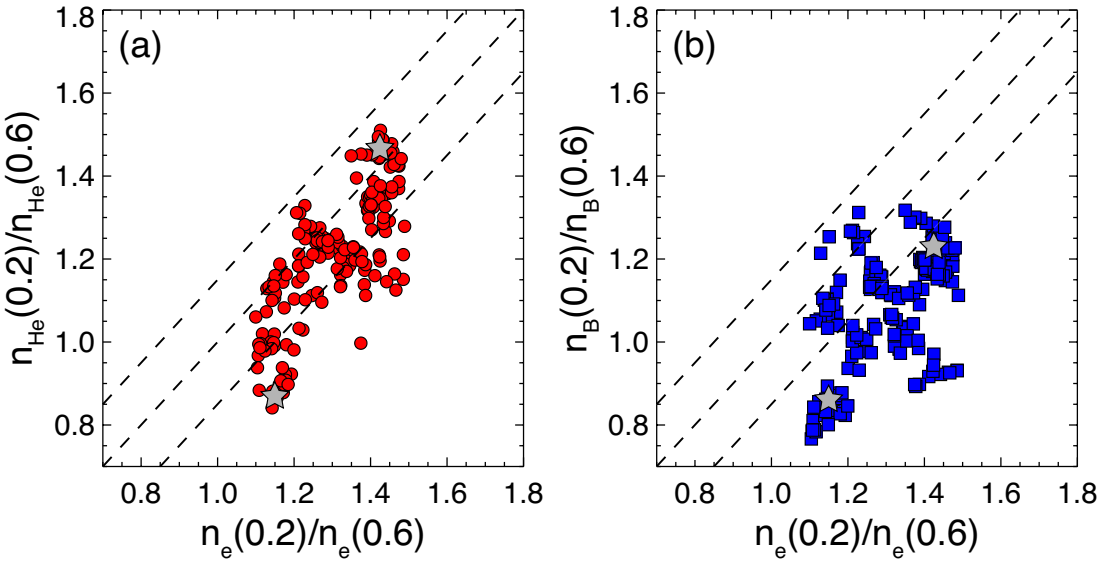

Figure 3. Peaking of the a) helium (red circles) and b) boron (blue squares) density profiles, defined as $n_Z(\rho_{tor} = 0.2)/n_Z(\rho_{tor} = 0.6)$ versus the peaking of the electron density profile $n_e(\rho_{tor} = 0.2)/n_e(\rho_{tor} = 0.6)$. The dashed lines indicate the band of experimental uncertainties, within which the impurity density profile can be considered as peaked as the electron density. The example profiles shown in Fig. 2 are indicated with stars.

and their gradients (see next section).

The application of central ECRH leads to an increase of the electron temperature and affects the peaking of the electron and impurity density profiles, also through its effect on the plasma collisionality (for electrons) and on the electron to ion temperature ratio (for impurities) (see Sec 2.1). The peaking of the helium, boron and electron density profiles is shown as a function of the applied ECRH power in Fig. 4. Two situations are presented: in the first, an ECRH power scan is performed on top of 2.5 MW of NBI power (Fig. 4a-b), while in the second, an ECRH power scan is performed on top of a higher level of NBI power of 7.5 MW (Fig. 4c).

With low background NBI power and low D-fuelling ($< 2 \cdot 10^{21} e/s$), shown in Fig. 4a, the peaking of the density profiles increases with increasing ECRH power for all species, but saturates at the highest powers. As such, the helium concentration $c_{\mathrm{He}} = n_{\mathrm{He}}/n_{\mathrm{e}}$ is flat with the exception of the higher ECRH power cases, in which the helium density is less peaked than the electron density. The boron density peaking is consistently lower than the electron density peaking and the peaking of the boron profile increases only slightly. With stronger D-fuelling ($> 2 \cdot 10^{21} e/s$), shown in Fig. 4b, the changes are stronger, also for boron. In the case of 7.5 MW of NBI, shown in Fig. 4c (D-fuelling $< 4 \cdot 10^{21} e/s$), the behavior is different with increasing ECRH power. At low ECRH heating fractions, the helium density is less peaked than the electron density, but approaches the electron density peaking with increasing ECRH power. The same holds for the boron density, which remains less peaked than the electron density at all power levels.

NBI heating leads to a decrease in collisionality and an increase of R/L_{T_i} and Mach number, due to the added NBI torque, and provides also ion heating. The use of off-

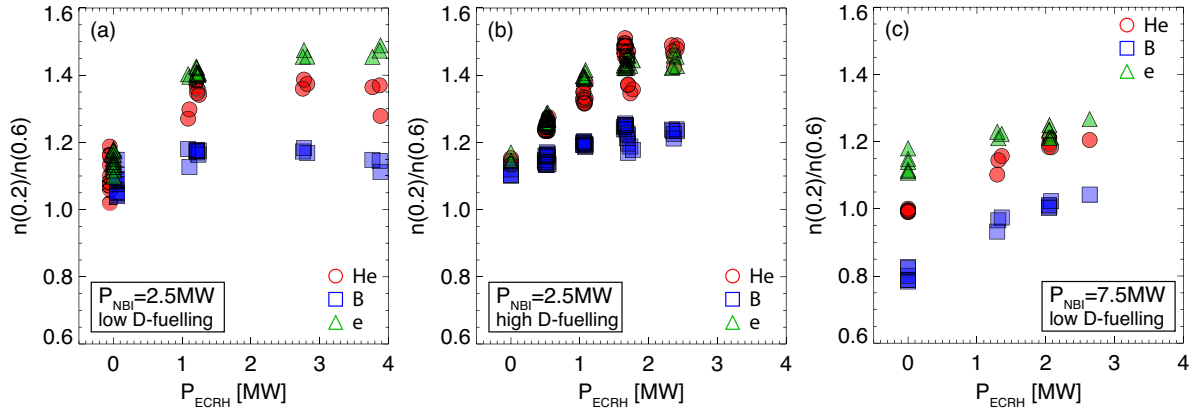

Figure 4. Peaking of the electron (green triangles), helium (red circles) and boron (blue squares) density profiles, defined as $n_X(\rho_{\rm tor}=0.2)/n_X(\rho_{\rm tor}=0.6)$, in different levels of the centrally applied ECRH power, a) with a background of NBI power of 2.5 MW and low D-fuelling, b) with a background of NBI power of 2.5 MW and high D-fuelling and c) with a background of NBI power of 7.5 MW and low D-fuelling.

axis neutral beam sources (numbered #6 and #7) is an additional, although limited, way to modify the gradient of the ion temperature and plasma rotation profiles. The behavior of the electron and impurity profiles with increasing NBI power is shown in Fig. 5. Again, two situations are presented: one with a minimum of ECRH (0.5 MW, Fig. 5a), usually applied to avoid tungsten accumulation in the plasma [24], and one at higher levels of ECRH power (1.0-1.4 MW, Fig. 5b). With $P_{ECRH} = 0.5$ MW, the peaking of the electron density profile is observed to increase with increasing NBI power, while a decreasing trend is observed at higher levels of ECRH power (1.0-1.4 MW). In both cases, the impurity density profiles become less peaked with increasing NBI power. The helium concentration profiles are flat at low levels of P_{NBI} and become hollow with dominant NBI heating. The boron concentration profiles are hollow in all cases, but become more hollow with dominant NBI heating.

Increasing the D-fuelling of the plasma generally leads to higher levels of electron density and, therefore, higher collisionality. A plasma discharge in which a scan of the D-fuelling was performed is shown in Fig. 6, where the points with low $P_{ECRH} = 0.5$ MW and high $P_{ECRH} = 1.7$ MW are shown in the left and right hand panels. With increasing D-fuelling, the peaking of the electron density profile is shown to decrease, at both levels of ECRH power. The opposite effect is observed for the impurities. The impurity concentration profiles become more peaked with increasing plasma fuelling. This change, however, is not as obvious in the case of helium at high ECRH power levels. Furthermore, the peaking of helium and electron density is much higher in the high P_{ECRH} cases in comparison to the low P_{ECRH} cases, while for boron this increase is not as pronounced.

Discharges were also performed at higher plasma currents, namely also at 0.8 MA and 1.0 MA, compared to the 0.6 MA plasma current which was used for the largest part of the database. However, due to operational constraints, the discharges at higher plasma currents also featured higher plasma densities. For this reason, a potential effect of the plasma current, and more fundamentally the q-profile and the magnetic shear, is obscured

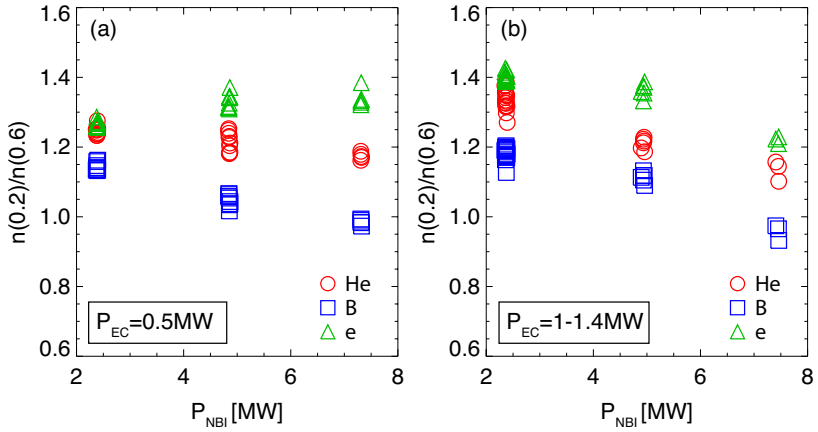

Figure 5. Peaking of the electron (green triangles), helium (red circles) and boron (blue squares) density profiles, defined as $n_X(\rho_{\rm tor}=0.2)/n_X(\rho_{\rm tor}=0.6)$, in different levels of the applied NBI power, with a background of ECRH power of a) 0.5 MW and b) 1.0-1.4 MW.

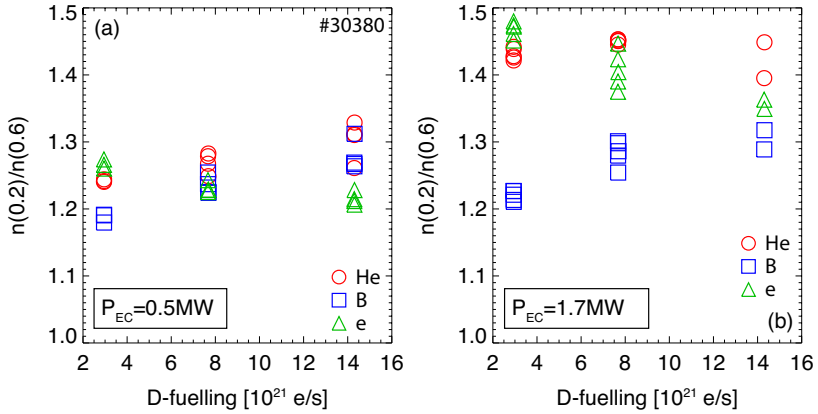

Figure 6. Peaking of the electron (green triangles), helium (red circles) and boron (blue squares) density profiles, defined equal to $n_X(\rho_{\rm tor}=0.2)/n_X(\rho_{\rm tor}=0.6)$, as a function of the D plasma fuelling with $P_{\rm NBI}$=2.5 MW and a) $P_{\rm ECRH}$=0.5 MW or b) $P_{\rm ECRH}$=1.7 MW.

by changes in plasma density and collisionality. A discussion on the effect of the q-profile shape on the impurity density profile shape expected from theory is given in the next section. Discharges with lower plasma current (0.4 kA) were proven to be unstable to the modulation of the neutral beams, needed for the subtraction of the passive emissions in the charge exchange spectra, and have not been included.

The observations described in this section show that the examination of the experimental data as a function of the actuators is insufficient for understanding and the physics parameters should be considered instead. Two of the main physics parameters that are affected by changes in the applied heating and fuelling are the ratio of the electron and ion temperatures and the plasma effective collisionality. In particular, considering also Fig. 4-6, the actuators have the following effects on the electron to ion temperature ratio and on the collisionality; when increasingly more $P_{\rm ECRH}$ is applied and T_e increases, T_e/T_i

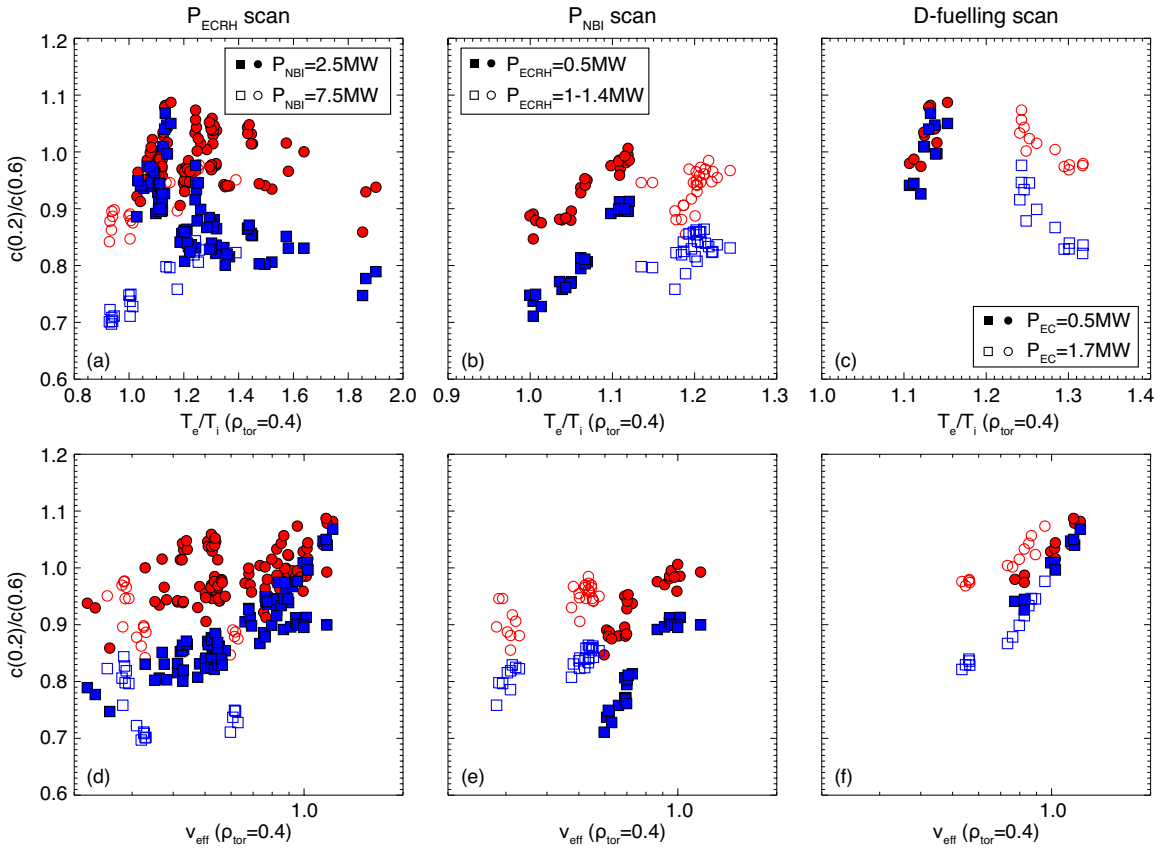

Figure 7. Peaking of the helium (red circles) and boron (blue squares) concentration profiles, defined equal to $c_X(\rho_{\rm tor}=0.2)/c_X(\rho_{\rm tor}=0.6)$ plotted against the ratio of the electron to ion temperature (plots (a)-(c)) and against the collisionality (plots (d)-(f)) for the $\rm P_{ECRH}$, $\rm P_{NBI}$ and D-fuelling scans, shown in Fig. 4, 5 and 6, respectively.

increases and $\nu_{\rm eff}$ decreases. With increasing $\rm P_{NBI}$, both parameters are found to decrease, while with additional D-fuelling, $\rm T_e/T_i$ decreases and $\nu_{\rm eff}$ increases. Here, the peaking of the impurity concentration is plotted versus these parameters in Fig. 7. The peaking of the impurity concentration profile can be used to describe the impurity density profiles in relation to the electron density profile. Concentration peaking of ~ 1 indicates that the impurity density profile is similar in shape to the electron density. For the majority of the points $\rm T_e/T_i$ is greater than 1 (Fig. 7a-c). In the $\rm P_{ECRH}$ scan, at high $\rm P_{NBI}$, the peaking of the impurity concentration profiles increases with increasing $\rm T_e/T_i$. Note, the high collisionality subset of these points corresponds to lower local electron temperatures at constant electron density. At low $\rm P_{NBI}$, the concentration profiles become less peaked with increasing $\rm T_e/T_i$, with the exception of helium at $\rm T_e/T_i$ approaching 1. In the $\rm P_{NBI}$ scan, the impurity concentration profiles become more peaked with higher $\rm T_e/T_i$ ratios. In the D-fuelling scan presented, the concentration profiles become more peaked or less peaked, for low and high $\rm P_{ECRH}$, respectively. With increasing collisionality (Fig. 7d-f), the impurity concentration profiles become flatter (peaking closer to 1), because the impurity density profiles peak and approach the electron density profile peaking, in all cases, with the exception of the $\rm P_{ECRH}$ scan cases at high $\rm P_{NBI}$. Considering the low collisionality regimes expected for ITER, this anticipates that there is no danger for low-

Z impurity accumulation.

3. Comparison with the modelling predictions

As shown in the previous section, examining the response of the impurity density profiles to the experimental actuators is not sufficient to understand the transport processes at play. A more comprehensive look at the physics and the local plasma parameters is required. To identify the underlying physics mechanisms at work, simulations of the neoclassical and turbulent transport in these plasmas were performed and compared to the experimental observations. These comparisons also constitute an experimental validation of the state-of-the-art theoretical understanding of impurity transport.

Neoclassical transport theory provides the necessary corrections to the classical collisional transport theory, taking into account the toroidal geometry of tokamak plasmas. It cannot, however, by itself describe the radial cross-field transport of impurities and the experimental observations. Around mid-radius, low-Z impurity transport is dominated by turbulent processes and neoclassical transport is expected to be negligible [24, 2] in comparison to the turbulent contributions.

To ensure that neoclassical transport is negligible at the location of interest, the neoclassical diffusion coefficients and drift velocities are calculated for the database using NEOART [25, 26]. NEOART provides the neoclassical transport parameters consisting of a classical, a Pfirsch-Schlüter, and a banana-plateau term. All collisions between all impurities (here He, B and W) and between the impurities and the main ions are considered. Impurity density profile gradients calculated taking only the neoclassical transport into account are compared with those obtained from the experiment at $\rho_{tor} = 0.5$ in Fig. 8. As expected for this location, neoclassical transport does not seem able to explain the measurement. It predicts R/L_{n_B} in the range of -5 to 10, which are not observed in the experiment. The neoclassical prediction for helium seems better in comparison to the boron, but still with large discrepancies. However, even if the neoclassical prediction for v/D were good, the absolute values of v and D separately are important. The total v and D include also turbulent contributions, which are more important than the neoclassical ones as it will be shown below.

The impurity particle flux due to turbulent transport processes is given by the diagonal diffusive flux, the thermodiffusion, the rotodiffusion and the pure convective parts, as follows [27, 28, 4, 29, 30]:

$$\frac{R\Gamma_I}{n_I} = D_{d,I}\frac{R}{L_{n_I}} + D_{th,I}\frac{R}{L_{T_I}} + D_{u,I}u'_I + RV_{p,I}, \tag{1}$$

where $\mathrm{R/L_X}$ are the local normalised logarithmic gradients and u' is the radial gradient of the toroidal plasma velocity. D denotes the respective diffusion coefficients and $V_{p,I}$ denotes the pure convective velocity. Note, the last three terms correspond to the total convective part. The diagonal diffusion depends on charge Z and mass A of the impurity. Thermodiffusion has an inverse charge dependence $(1/Z)$ and is therefore more important for lower-Z impurities. Rotodiffusion has mainly a A/Z dependence and pure convection has mainly a $1/Z$ dependent and a constant part. Looking at different impurities, such as

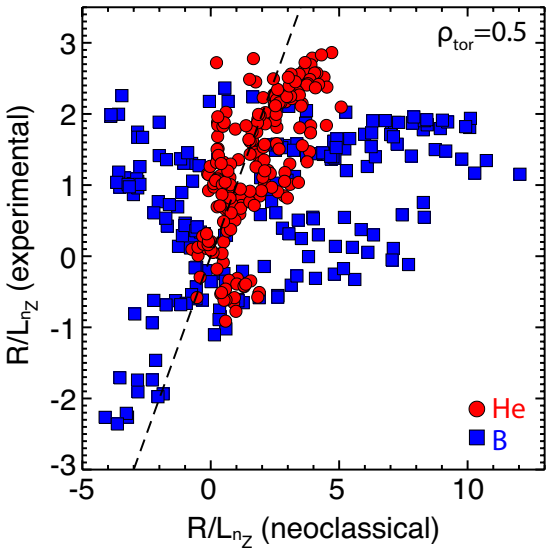

Figure 8. R/L_{n_B} (blue squares) and $R/L_{n_{He}}$ (red circles) from the experiment are compared with the prediction based on neoclassical transport alone, at $\rho_{tor} = 0.5$.

helium (A/Z=4/2) and boron (A/Z=11/5), differences are expected, primarily from the thermodiffusive part.

Assuming only turbulent transport contributions, as is expected in the confinement region of the plasma and especially around the mid-radius for low-Z impurities, no impurity sources and steady state conditions, the impurity density logarithmic gradient can be derived from (1), with $\Gamma_I = 0$:

$$\left.\frac{R}{L_{n_I}}\right|^{turb} \simeq -\left(\frac{D_{th,I}}{D_{d,I}}\frac{R}{L_{T_I}} + \frac{D_{u,I}}{D_{d,I}}u'_I + \frac{RV_{p,I}}{D_{d,I}}\right). \tag{2}$$

The assumption of zero impurity flux is justified by the fact that helium and boron are not externally added to the plasma, while any wall source does not have an effect on the impurity density gradients at the plasma mid-radius, as their ionisation source profiles reach at most $\rho_{pol} \sim 0.95$.

Impurity transport caused by electrostatic plasma turbulence, which is non-linear in nature, can be studied within a fluid or a gyrokinetic approach with a variety of non-linear and quasi-linear models. The modelling of the turbulent transport in the database presented here was performed with the gyrokinetic code GKW [31, 32]. GKW is a Eulerian, flux-tube code which can solve the nonlinear gyrokinetic Vlasov-Maxwell equations. Here, the local flux-tube version of the code was used. The flux surface average (denoted by $\langle ... \rangle_{fs}$) of the quasi-linear particle flux for species I is given by:

$$\Gamma_{I_{QL}} = \left\langle \int d^3v \; f_I \frac{\overrightarrow{B} \times \nabla \mathcal{L}}{B^2} \cdot \nabla \psi \right\rangle_{fs}. \tag{3}$$

Here, f_I is the perturbed distribution function and ψ represents the radial coordinate. $\mathcal{L} = \tilde{\Phi} - v_{\parallel}\tilde{A}_{\parallel}$, where $\tilde{\Phi}$ is the gyro-averaged perturbed electrostatic potential and $A_{\parallel}$ is the gyro-averaged parallel component of the vector potential. The term $\tilde{\Phi}$ corresponds

to the $E \times B$ transport and $\tilde{A}_{\|}$ to the magnetic flutter transport. The quasi-linear weighted flux is given by $\Gamma_{QL}/\left|\tilde{\Phi}\right|^2$. Normalised logarithmic impurity density gradients are derived from linear and nonlinear simulations, making use of $\Gamma_I = 0$. The rotodiffusive contribution to the turbulent transport and the Coriolis force are included [29, 33, 32, 34]. Centrifugal effects are not included in these simulations, as they are negligible for light impurity species such as helium and boron. Linear simulations show good agreement with the nonlinear ones, as shown in [4], and are, therefore, the main workhorse for the investigations shown here, due to the size of database. GKW contains, like other codes, all physics commonly used in the local description. A benchmark between GKW and GENE, though without the inclusion of impurities, is reported in [35]. Analogous results for impurities as those presented here have been also obtained with GS2 [2] and GENE [6]. Assuming trace helium and boron in the plasma, the transport coefficients depend solely on the background plasma turbulence. This holds for the database in question, as the concentrations of boron and helium are $c_{\mathrm{B}} < 0.8\%$ and $c_{\mathrm{He}} < 1.5\%$, respectively, and together are the dominant low-Z impurity species after a boronisation at ASDEX Upgrade.

The gyrokinetic simulations have been performed over a spectrum from normalised binormal wavenumbers $k_y\rho = 0.15$ to 0.65. Spectral averages have been performed considering spectra of the saturated electrostatic potential that are close to those obtained in nonlinear simulations in [3]. Electromagnetic effects are included. The simulations are performed with $n_\mu = 8$ grid points for the magnetic moment, $n_{v_\|} = 32$ grid points for the parallel velocity and $n_s/n_p = 30$ grid points along the magnetic field line per poloidal turn. Turbulent diagonal and off-diagonal impurity transport coefficients can be derived from such simulations, the combination of which provides the simulated normalised logarithmic impurity density gradients to be compared to the experimentally obtained values.

The results of the gyrokinetic modelling for the database are shown in Fig. 9. The predicted $R/L_{n_{\mathrm{B}}}$ and $R/L_{n_{\mathrm{He}}}$ and the off-diagonal contributions to the turbulent transport of the impurities are plotted as a function of the frequency of the most unstable mode ω_r and at $\rho_{\mathrm{tor}} = 0.5$. Positive values of ω_r correspond to an ITG dominated regime and negative values correspond to a TEM dominated regime. At mid-radius, the database is primarily ITG dominated, but covers the range $-0.4 < \omega_r < 0.9$. The trends observed for the thermodiffusive, rotodiffusive and pure convective terms are consistent with those previously obtained for boron in [2], furthermore, clear differences are observed for the two impurities analysed here. The pure convective term (d) is negative at all frequencies, meaning that it always leads to peaking of the profiles. Larger absolute values are predicted with increasing ω_r. Similar behavior of the convective term is predicted for both helium and boron. The rotodiffusive term (c) is positive (outward) in the ITG regime and negative (inward) in the TEM dominated regime. Again, similar behavior is predicted for the two impurities, but the rotodiffusive term is stronger for boron than for helium. The thermodiffusive term (b) is also directed outwards in ITG dominated regimes, leading to flattening of the profiles, and reverses sign as the regime transitions from ITG to TEM leading to inward transport and peaking of the profiles. Here, a clear difference between the two impurities is predicted. Due to its inverse charge dependence,

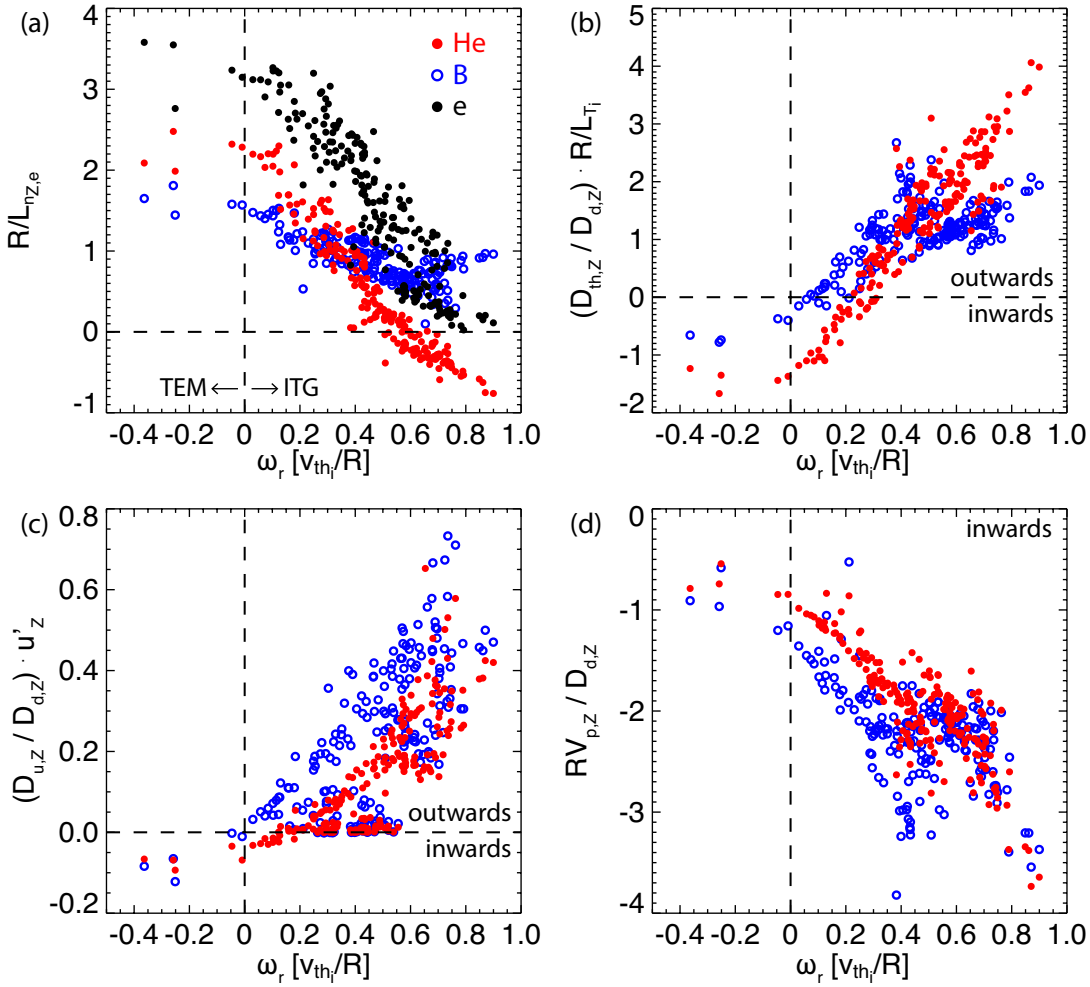

Figure 9. Predicted $R/L_{n_{\rm B}}$ (blue open circles), $R/L_{n_{\rm He}}$ (red filled circles) and experimental (input) R/L_{n_e} (black) (a) and turbulent contributions to the impurity transport, namely (b) the thermodiffusive term, (c) rotodiffusive term and (d) the pure convection term for each impurity at $\rho_{tor} = 0.5$. Note, the minus sign in Eq. (2) is not represented.

the thermodiffusive contribution to the fluxes is expected to be more important for lower-Z impurities. As a result, thermodiffusion is expected to be smaller in absolute values than the pure convection in the case of boron, but becomes much more significant in the case of helium. Mainly as a result of the thermodiffusive term, the gyrokinetic modelling predicts helium profiles that are significantly flatter (or even hollow) than for boron in the ITG dominated regime and slightly more peaked than the boron profiles as the transition to the TEM regime occurs. This can be seen in the GKW predictions of $R/L_{n_{\rm He}}$ and $R/L_{n_{\rm B}}$ shown in Fig. 9(a). Similar observations are made further into the plasma core, for $\rho_{tor} = 0.3$ (not shown).

The GKW predictions of R/L_{n_Z} at $\rho_{tor} = 0.5$ are compared with the experimental ones in Fig. 10. The predicted $R/L_{n_{\rm He}}$ (red circles) are close to the experimental one in a subset of the database, but in many cases the experimental helium density profiles are more peaked than theory predicts. The experimental $R/L_{n_{\rm B}}$ (blue squares) are also

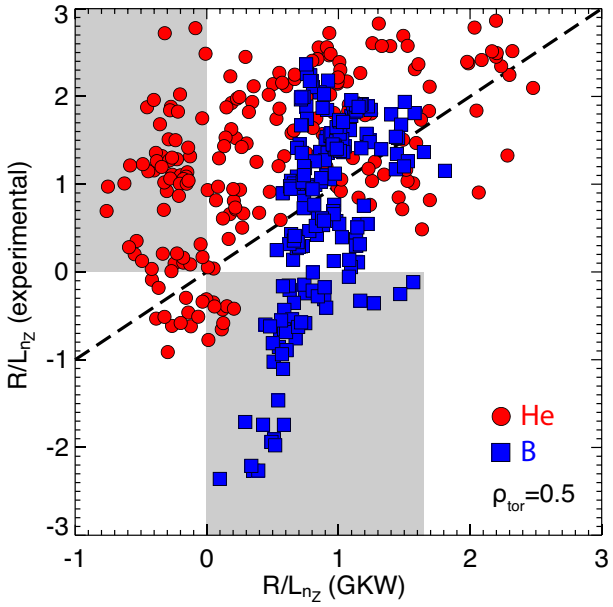

Figure 10. The experimentally deduced local normalised logarithmic gradient of the helium density $R/L_{n_{\mathrm{He}}}$ (red circles) and of the boron density $R/L_{n_{\mathrm{B}}}$ (blue squares) plotted against the prediction obtained with GKW at $\rho_{\mathrm{tor}} = 0.5$. The grey shaded areas indicate the cases for which the modelling predicts the opposite sign.

not reproduced in the majority of the cases. In particular, the measured hollow boron profiles are not reproduced as GKW predicts flat to peaked profiles, consistent with [3]. The cases where the sign of the predicted $\mathrm{R/L_{n_Z}}$ is opposite are highlighted with the grey areas. They provide a strong indication that the theoretically predicted convection is incorrect. Nevertheless, this does not imply that the predicted diffusion is correct.

Both turbulent and neoclassical transport mechanisms define the impurity density. Therefore, the local normalised logarithmic impurity density gradient is given by the ratio of the total convection to the total diffusion, taking into account both turbulent (turb) and neoclassical (NC) transport, assuming that the total impurity particle flux is zero:

$$\frac{R}{L_{n_I}} = -\frac{RV_I^{turb} + RV_I^{NC}}{D_{d,I}^{turb} + D_{d,I}^{NC}}. \tag{4}$$

The turbulent and neoclassical contributions are compared for the database by considering the diagonal diffusion coefficients, plotted as a function of the electron to ion temperature ratio in Fig. 11 at $\rho_{tor} = 0.5$. Following the approach in [2] and assuming that the ratio of the transport coefficients to the heat conductivity is weakly dependent on the turbulent transport levels [4], the turbulent diffusion coefficients are normalised with the effective ion heat conductivity $\chi_{i,turb}$ which is calculated by the GKW simulation, while the neoclassical diffusion coefficient is normalised with the anomalous part of the power balance ion heat conductivity, defined as $\chi_{i,an} = \chi_i^{PB} - \chi_i^{NC}$, obtained from TRANSP simulations [36]. This is done to account for possible discrepancies (up to an order of magnitude) between the actual and simulated fluxes due to the sensitivity of the modelling on the input (here, $\chi_{i,turb}$ is an order of magnitude smaller than $\chi_{i,an}$). It is observed that the turbulent diffusion is larger than the neoclassical by two orders of magnitude or more

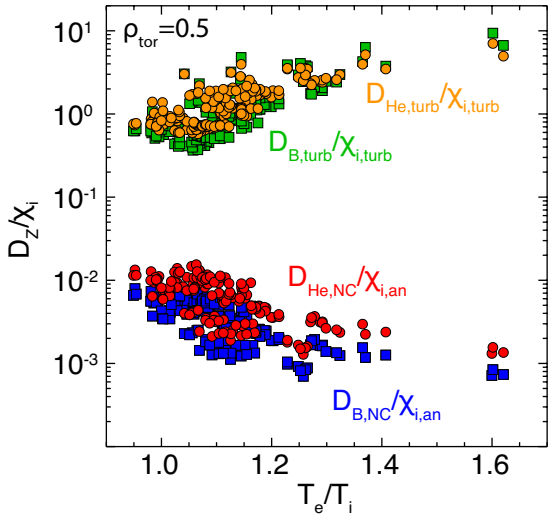

Figure 11. The turbulent and neoclassical diffusion coefficients at $\rho_{tor} = 0.5$ for helium (red, orange circles) and boron (blue, green squares), normalised to the effective ion heat conductivity obtained from the GKW calculations and the anomalous part of the power balance ion heat conductivity, respectively.

at $\rho_{tor} = 0.5$. Further into the plasma core, for example for $\rho_{tor} = 0.3$ (not shown), neoclassical transport starts to become important (and more important for helium than for boron) and the neoclassical diffusion is in this case only one order of magnitude smaller than the turbulent diffusion. It can, therefore, be concluded that the neoclassical contribution to the particle transport is negligible for both impurities at mid-radius in this database, but can become important further into the plasma core.

3.1. Experimental and modelled $R/L_{n_{\mathrm{He}}}$ and $R/L_{n_{\mathrm{B}}}$

The experimentally obtained values of the local normalised logarithmic gradients $R/L_{n_{\mathrm{B}}}$ and $R/L_{n_{\mathrm{He}}}$ are now compared to the theoretical predictions. The discussion focuses on $\rho_{tor} = 0.5$, where turbulent transport was shown to be dominant (see previous section). In the following figures, the experimental values are compared to those derived from the modelling of the turbulent transport. As explained above, the comparison between the experiment and the theoretical predictions at this location does not change significantly with the inclusion of neoclassical components.

A comparison of the experimental and predicted local normalised logarithmic gradients of helium and boron at $\rho_{\mathrm{tor}} = 0.5$ is shown in Fig. 12 for two ECRH scans with fixed background NBI powers. The local normalised logarithmic gradients at $\rho_{\mathrm{tor}} = 0.5$ of He in the top row and B in the bottom row are plotted against that of the electron density, the ion temperature, and the radial gradient of the toroidal plasma velocity. Note, however, that a one-to-one relation between R/L_{n_Z} with these parameters cannot be derived. The datasets plotted here are not independent. For example, as high R/L_{n_e}, low R/L_{T_i} and low u' all occur together, it is not possible to disentangle the different effects from these plots. R/L_{n_Z} is determined by the relative magnitude of the terms in Eq. 2, namely the thermodiffusion, rotodiffusion and pure convection. The coefficients

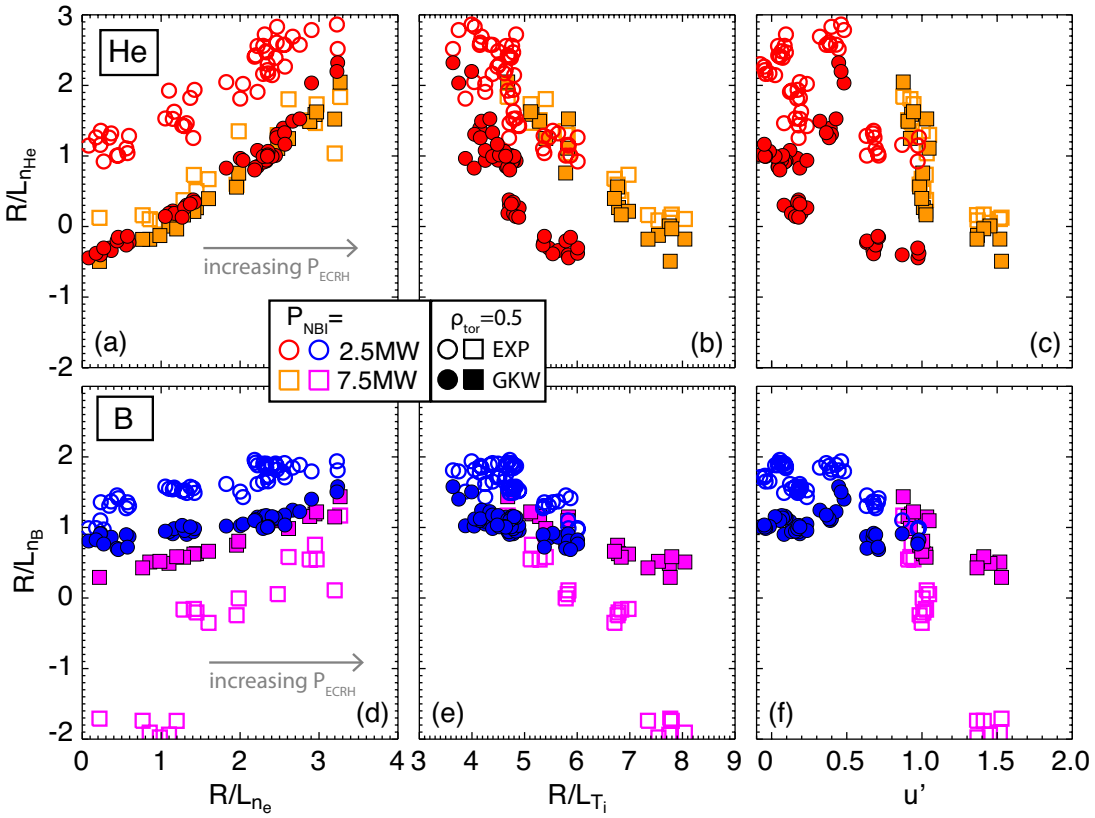

Figure 12. The local normalised logarithmic gradient of the helium density $R/L_{n_{\mathrm{He}}}$ (plots (a)-(c)) and of the boron density $R/L_{n_{\mathrm{B}}}$ (plots (d)-(f)) versus R/L_{n_e}, R/L_{T_i} and u' (for D) at $\rho_{\mathrm{tor}} = 0.5$. The database points correspond to various levels of centrally applied $\mathrm{P_{ECRH}}$ (see Fig. 4) on top of 2.5 MW (red and blue circles) and 7.5 MW of $\mathrm{P_{NBI}}$ (orange and magenta squares). The open symbols corresponds to the experimental gradients and the filled symbols correspond to the predictions obtained with quasilinear GKW simulations.

encountered in each term depend on the mass, charge, impurity temperature and the parameters of the background plasma [4]. The experimental gradients are shown with open symbols and the GKW predictions with filled symbols. With low NBI power (2.5 MW), the trends between experiment and theory are similar. However, both impurity gradients are underpredicted by GKW. The prediction is closer for B, even within error bars, as reported in previous AUG results [3]. Also, locally hollow He density profiles ($R/L_{n_{He}} < 0$) are predicted for experimentally peaked cases. With increased NBI power (7.5 MW), He is very well described by the theoretical predictions, but the peaking of B is in this case overpredicted. Very hollow experimental B density profiles are observed in the experiment, which are not reproduced by the gyrokinetic simulations.

The gyrokinetic modelling predictions are shown to over- or under-predict the local normalised logarithmic gradients of both impurities depending on the local parameters. When the predictions are too low in comparison to the experiment, this is suggestive of a missing inward contribution or an outward contribution that is too high, and vice versa when the predictions are too high. In the case of B, looking at the data points for both NBI power levels, it can be argued that the modelling does not capture the

dependence on R/L_{T_i} and u', in other words the thermodiffusion and rotodiffusion terms, correctly. However, as both parameters are highly correlated in the experiment, it is not possible to disentangle the two effects. While the cases with lower R/L_{T_i} and u' are underpredicted by the simulations, the cases with higher R/L_{T_i} and u', which are closer to the parameter space explored in studies of C transport in H-mode plasmas in JET with the C-wall, are overpredicted by the simulations, as also reported in [37]. Furthermore, the gradients of the very hollow boron density profiles observed with $P_{NBI} = 7.5$ MW are largely overpredicted by the modelling. These profiles correspond to cases with high P_{NBI} without ECRH and are characterised by high fast ion densities (and fast ion $\beta = 0.4 - 0.7\%$), in combination with high values of R/L_{T_i} ∼7-8 and u' ∼1.5, indicating possible elements might be missing in the simulations.

In general, the qualitative trends are reproduced when comparing the modelling predictions with the experiment, even if the modelling does not always reproduce the observed values. For example, the increasing $R/L_{n_{\mathrm{He}}}$ and $R/L_{n_{\mathrm{B}}}$ observed in the experiment with increasing ECRH at low NBI power is also observed in the modelling results. For increasing NBI power at constant ECRH power, however, the experimental trends are not captured at all by the quasilinear modelling. This is shown in Fig. 13. Here, cases with low and medium P_{ECRH}, 0.5 MW and 1-1.4 MW are shown. Note, these are the same experimental data as shown in Fig. 5. GKW predicts increasing $R/L_{n_{\mathrm{He}}}$ with increasing R/L_{n_e} (and R/L_{T_i} and u'), while the experimental $R/L_{n_{\mathrm{He}}}$ decreases. Negative gradients are predicted for helium in cases of experimental gradients higher than 1. Furthermore, GKW predicts almost the same $R/L_{n_{\mathrm{B}}}$, despite the variation in R/L_{n_e}, R/L_{T_i} and u'. Similar observations are made when considering the trends of the experimental and predicted $R/L_{n_{\mathrm{He}}}$ and $R/L_{n_{\mathrm{B}}}$ versus the input torque and the fast-ion β.

As the injected NBI power is increased, the plasma rotation and u' increases. According to the theoretical understanding of the rotodiffusion mechanism, at higher plasma rotation and higher u' values, less peaked impurity density profiles are expected. A strong rotation gradient causes a flattening or even hollowing of the impurity density profiles. This is indeed confirmed experimentally for both impurities. However, looking at the modelling prediction, it is found that almost no variation of R/L_{n_B} is expected, while an opposite behavior to the one experimentally observed is predicted for helium. Examining each term contributing to the turbulent transport shown in Fig. 14 (top row), as predicted by the gyrokinetic modelling, namely the thermodiffusive term (directed outwards in ITG), the rotodiffusive term (also directed outwards) and the pure convective term (always directed inwards) for the P_{NBI} scan in discharge #30379 (see Fig. 1), a few observations can be made. From low to high P_{NBI}, the trends between the experimental and predicted gradients do not agree, as also shown in Fig. 13. R/L_{T_i} is increased from 5.9 to 6.7 and u' from 0.7 to 1.0, from the low to the high P_{NBI} points. The reduction in absolute value of the outward thermodiffusive flux for helium, with increasing P_{NBI}, is larger than the reduction of the inward convective flux, leading to a more peaked predicted helium profile, while the rotodiffusive contribution is only slightly changing (from -0.17 to -0.21). For boron, the changes in the outward directed rotodiffusive (from -0.24 to -0.38) and thermodiffusive terms compensate each other, leading to almost no variation

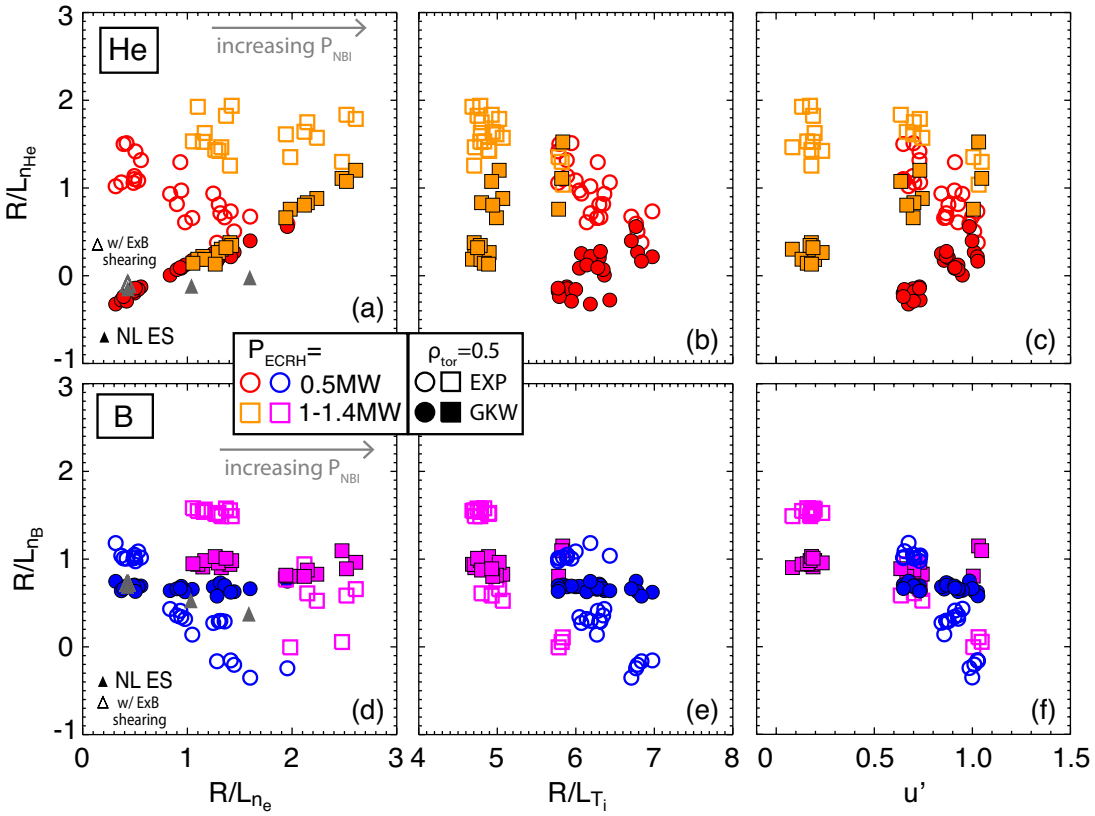

Figure 13. The local normalised logarithmic gradient of the helium density $R/L_{n_{\mathrm{He}}}$ (plots (a)-(c)) and of the boron density $R/L_{n_{\mathrm{B}}}$ (plots (d)-(f)) versus R/L_{n_e}, R/L_{T_i} and u' (for D) at $\rho_{\mathrm{tor}} = 0.5$. The database points correspond to various levels of injected $\mathrm{P_{NBI}}$ (see Fig. 5) on top of 0.5 MW (red and blue circles) and 1.0-1.4 MW of $\mathrm{P_{ECRH}}$ (orange and magenta squares). The open symbols corresponds to the experimental gradients and the filled symbols correspond to the predictions obtained with quasilinear GKW simulations. The triangles correspond to non-linear electrostatic ("NL ES") gyrokinetic simulations with GKW without (filled) and with (open) the E × B shearing.

of $R/L_{n_{\mathrm{B}}}$. However, it is not possible to disentangle the changes in R/L_{T_i} and u' in the experiment and to conclude on the term that is not properly captured by the gyrokinetic modelling. In the bottom row of Fig. 14, two instances from #33400 are shown, with a large change in u' from ∼1.0 to ∼1.7. For these two cases, $\mathrm{P_{NBI}}$ = 7.5 MW and 10 MW, $\mathrm{P_{ECRH}}$ = 1.3 MW and 0 MW, and R/L_{T_i} ∼5.8 and 8.2, respectively. It is observed that, despite the large change in u', the change in the rotodiffusion contribution is small and the predicted profile peaking is defined mainly by the interplay between the pure convection and the thermodiffusion. This leads to satisfactory agreement between experiment and prediction for helium, but not for boron.

A limited set of non-linear electrostatic gyrokinetic simulations with GKW were performed, over a spectrum from normalised binormal wavenumbers $k_y\rho = 0.0625$ to 2 (filled triangles in Fig. 13). In the non-linear results, $R/L_{n_{\mathrm{He}}}$ does not increase with increasing R/L_{n_e} as in the quasi-linear results and the value of $R/L_{n_{\mathrm{He}}}$ is still too low in comparison to the experiment, while $R/L_{n_{\mathrm{B}}}$ shows a slightly negative slope. The inclusion of E × B shearing for one point (open triangle) did not make a significant difference. The

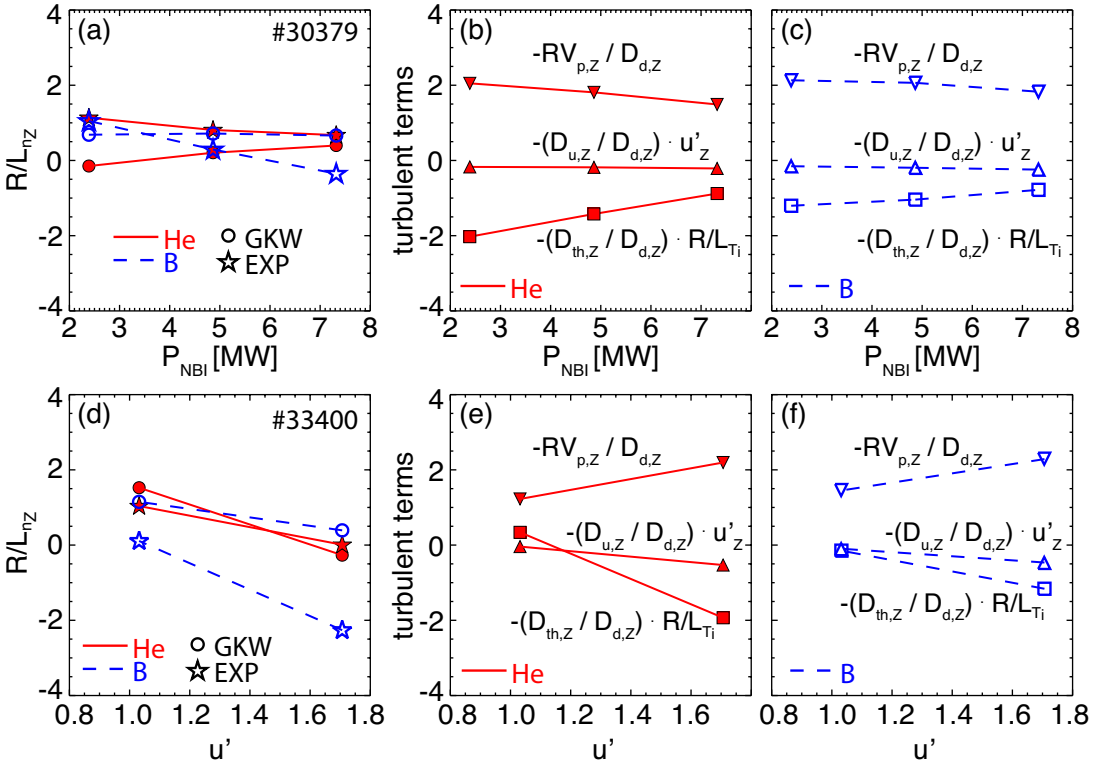

Figure 14. a) A subset of the experimental (stars) and predicted (circles) $R/L_{n_{\rm He}}$ and $R/L_{n_{\rm B}}$ are shown as as a function of the NBI power scan in #30379. Red filled symbols and solid lines correspond to He and blue open symbols and dashed lines to B. On the right, the turbulent terms defining the impurity gradients in the left plot are shown, namely, the thermodiffusive (squares), rotodiffusive (upward triangles) and pure convective (downward triangles) terms are shown for b) He and c) B. d) A subset of the experimental and predicted $R/L_{n_{\rm He}}$ and $R/L_{n_{\rm B}}$ are shown as a function of u' in #33400 (same notation), with the corresponding turbulent terms in plots (e) and (f). R/L_{T_i} is $\sim$5.8 and $\sim$8.2 in the low and high u' cases, respectively.

electron and ion heat fluxes obtained with the non-linear simulations are close to the experimental ones, with the exception of the point with the highest $\rm P_{NBI}$=7.5 MW, as electromagnetic stabilisation and fast ions are not included. Extensive non-linear work is ongoing to evaluate the impact of such mechanisms on impurity transport.

The uncertainty on the local normalised logarithmic gradients calculated from the experimental data can be quite large. The uncertainty on the measured density profile, the plasma major radius and flux surface averaged plasma minor radius contribute to the uncertainty of the experimental R/L_{n_Z}. The last two are obtained from the magnetic equilibrium reconstruction and an accurate estimation of the error is not straightforward. Assuming a σ in the order of 10% on the measured impurity densities and for the region $\rho_{\rm tor} = 0.4 - 0.6$, one can consider Gaussian distributions around the measurement values and estimate the uncertainty on the gradients by linear fits (see [2] for a discussion). The mean $\Delta(R/L_{n_Z})$ in the database is then found to be ~ 2.3 for both impurities, with higher values for flatter profiles, and lower for more peaked profiles. For a larger uncertainty on the measurement, and/or a smaller region used for the average (for the plots

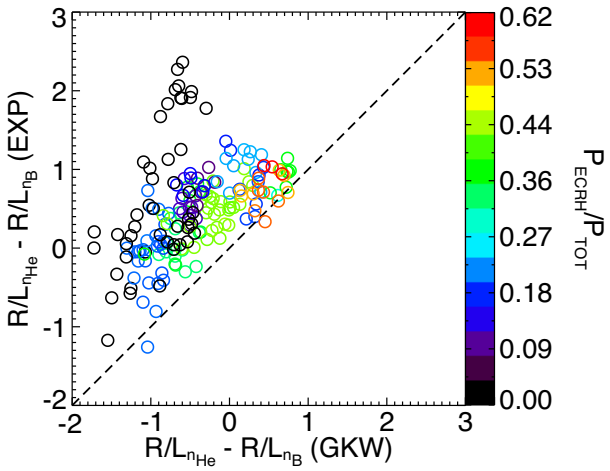

Figure 15. Differences between the $R/L_{n_{\mathrm{He}}}$ and $R/L_{n_{\mathrm{B}}}$ at $\rho_{\mathrm{tor}} = 0.5$ observed in the experiment and in the gyrokinetic simulations. The colors correspond to the ECRH heating fraction. Dominant NBI heating indicates higher R/L_{T_i} and u' values.

herein $\rho_{\mathrm{tor}} = 0.45 - 0.55$ was used), $\Delta(R/L_{n_Z})$ is larger. It is, therefore, recommended to examine trends between the experimental data and the theory predictions, as was done in the discussion above.

It is worthwhile to check if the differences between the two impurities are at least qualitatively reproduced by the gyrokinetic modelling. To visualise this, the difference between the helium and boron gradients observed in the experiment are plotted versus the difference in the predicted values in Fig. 15. The differences between $R/L_{n_{\mathrm{He}}}$ and $R/L_{n_{\mathrm{B}}}$ observed in the experiment are generally larger than the differences found in the simulations. The colors correspond to the different levels of ECRH heating fraction. The points with dominant NBI heating and with no or limited ECRH (darker colors) tend to be further away from the one-one line, with a subset of points for which $R/L_{n_{\mathrm{He}}} - R/L_{n_{\mathrm{B}}}$ is larger in the experiment, corresponding to the high levels of NBI power and no ECRH, representing the most extreme cases. Dominant NBI heating generally indicates higher R/L_{T_i} and u' values, pointing to the thermodiffusive and the rotodiffusive terms. In the theory, the difference between the two impurities is dominated by the thermodiffusive term, which does capture the general trend, but fails most strongly for the points with dominant NBI heating. Though not straightforward, this observation may indicate a missing element in the modelling of the outward convection.

3.2. Possible explanations for the discrepancies between experiment and modelling

The discrepancies observed between the experimental observations and the predictions of turbulent transport theory are outside error bars and indicate a missing element in the understanding of impurity transport processes. The following discussion aims to rule out a number of possible explanations that were considered in the course of this work.

Possible numerical issues of the quasi-linear modelling should first be considered. To confirm the chosen grid resolution ($n_\mu = 8$, $n_{v_\parallel} = 32$, $n_s/n_p = 30$), as series of simulations with increased resolution were performed at a single $k_y\rho \sim 0.42$ for a range of values of

the most unstable frequency ω_r. The simulation results for He are shown in Fig. 16 (the observations are the same for boron). It is shown that doubling the resolution of the magnetic moment grid and the parallel velocity ($n_\mu = 16$, $n_{v_\parallel} = 64$, $n_s/n_p = 30$) leads to very similar values for all components contributing to the local logarithmic helium density gradient $R/L_{n_{\mathrm{He}}}$. The largest differences are found for $\omega_r \sim 0$, but they remain very small. With double grid resolution along the field line ($n_\mu = 8$, $n_{v_\parallel} = 32$, $n_s/n_p = 60$), the results are almost identical (not shown).

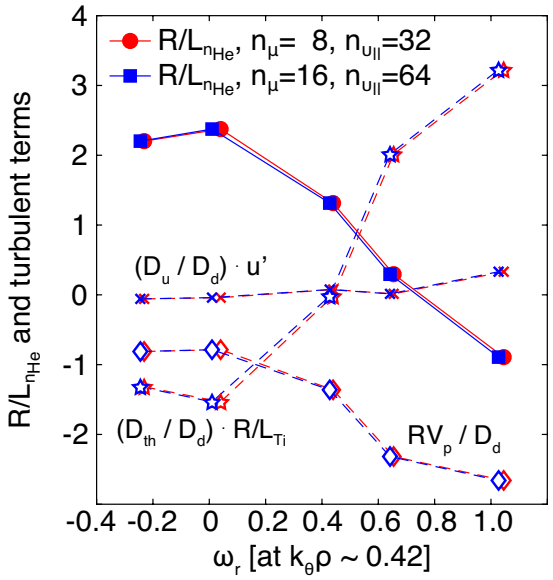

Figure 16. A subset of the $R/L_{n_{\mathrm{He}}}$ cases simulated with different grid resolutions for the magnetic moment and the parallel velocity (filled symbols) and the turbulent terms defining the helium density gradients (open symbols), namely the thermodiffusive (stars), rotodiffusive (crosses) and pure convective (diamonds) terms from the GKW simulations. Note, the minus sign in Eq. (2) is not represented.

The gyrokinetic simulations assume no impurity sources, or sinks. Helium and boron are not puffed, however, they are released from the tokamak wall, where they can be understood as "stored" during the boronisation process. The mechanisms governing the interaction of the plasma impurities with the tokamak wall and pumping chambers are complicated and the subject of a large field of research. Helium in particular is different than boron in this regard, as it is a recycling impurity that is not actively pumped by the cryopump at ASDEX Upgrade (only limited pumping from the turbopumps). Nevertheless, any wall source would contribute to the level of He content in the plasma, but is not expected to influence the local transport at mid-radius. Studies have shown that a core particle source, as will be the case in a reactor with fusion produced helium in the plasma core, has little effect on the helium density profile peaking [4]; this effect depends, however, on the helium density itself, and would become visible if the density is low enough and the pumping efficiency is high, while recycling determines mostly the helium concentration.

Another assumption made in the modelling is that the impurities are present in the plasma only as traces. The concentrations of boron and helium in the database are low

($c_{\mathrm{B}} < 0.8\%$ and $c_{\mathrm{He}} < 1.5\%$). When $R/L_{n_Z} > 0$, higher impurity concentrations lead to the stabilisation of ITG turbulence and a reduction in the growth rate γ. Thermodiffusion, the main outward convection contribution, has a $1/\gamma^2$ dependence and, therefore, increases with higher impurity concentrations, resulting to flatter profiles. When $R/L_{n_Z} < 0$, increasing impurity concentrations lead to the destabilisation of ITG and an increase of γ. Thermodiffusion then decreases, resulting to more peaked profiles. In Fig. 17, the theoretical predictions of the local normalised logarithmic impurity gradients are shown for the deviation from the trace assumption for a case in which the peaking of both impurities is underpredicted. The effect is not found to be large and it reduces the predicted peaking of the impurity density profiles, bringing the prediction further from the experiment.

Since the modelling is not able to reproduce the experimental gradients for the impurities, a justifiable question is whether the local normalised logarithmic gradients of the electron density profiles can be predicted in these cases. This was checked for a subset of the database, following the method outlined and used in [2]. The local normalised logarithmic electron density gradient was scanned in quasi-linear GKW simulations without impurities. The predicted R/L_{n_e} is obtained solving:

$$\frac{\Gamma_{\mathrm{turb(GKW)}}}{Q_{\mathrm{turb(GKW)}}} = \frac{\int_{\rho_{tor}=0.5}^{1} S_{\mathrm{NBI}} dV - \Gamma_{\mathrm{Ware}}}{Q_{\mathrm{heat(exp)}} - Q_i^{\mathrm{NC}}}, \tag{5}$$

where $\frac{\Gamma_{\mathrm{turb(GKW)}}}{Q_{\mathrm{turb(GKW)}}}$ is the ratio of the turbulent particle flux to the total turbulent heat flux, as obtained from GKW, S_{NBI} is the NBI particle source, Γ_{Ware} is the particle flux due to the Ware pinch, $Q_{\mathrm{heat(exp)}}$ is the integral of the total heating power density and Q_i^{NC} is the neoclassical ion heat flux. Satisfactory agreement is found between the predicted and experimental R/L_{n_e}, shown in Fig. 18, with a deviation up to about 30%, as also reported in [2].

One of the most important sensitivities of the gyrokinetic modelling is the uncertainty of the input magnetic equilibrium. The sensitivity of the gyrokinetic simulations to

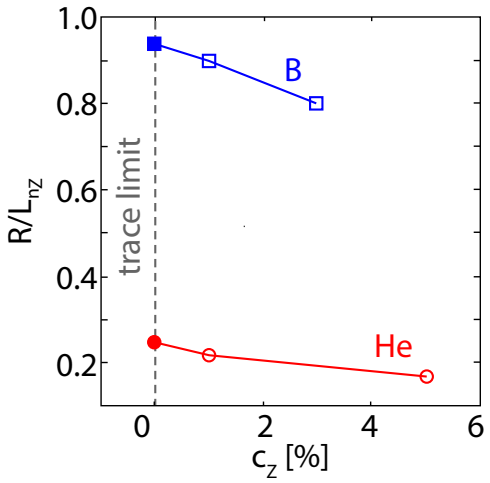

Figure 17. Effect on the predicted local normalised logarithmic impurity gradient, when diverging from the trace limit assumption.

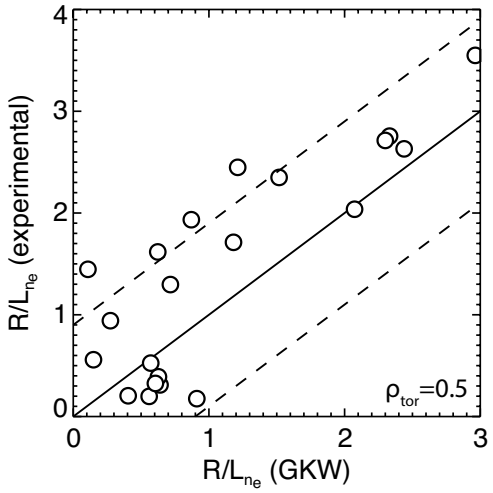

Figure 18. Experimental versus modelled R/L_{n_e} for a subset of the database. The figure includes instances from discharges with both an ECRH and an NBI power scan. The dashed lines indicate the 30% uncertainty.

the input magnetic shear and safety factor has been studied in detail in [3]. For the discharges in this database, the magnetic equilibrium is reconstructed from magnetic measurements. No direct measurement of the safety factor is available for these discharges. A pressure constrained magnetic equilibrium [38, 23], using the sawtooth inversion radius as a constraint for the $q = 1$ surface, can also be used as input. In Fig. 19, the local normalised logarithmic gradient prediction is shown as a function of the local magnetic shear, for two equilibria (referred to as "standard" and "improved," respectively), as well as for an artificial shear scan, using the local geometry Miller parametrisation [39] to vary the input shear. For the case shown here, $R/L_{n_{\mathrm{He}}}$ and $R/L_{n_{\mathrm{B}}}$ are underpredicted by the simulation. The predicted gradients vary with the different shear levels, as expected. But, most importantly, different behavior is found for the two impurities. With increasing shear (and also using the "improved" instead of the "standard" equilibrium), the prediction comes closer to the experiment for B, but the opposite holds for He. As mentioned earlier, attempts to reproduce this difference between the peaking of the two impurities experimentally were not successful, as the main experimental handle on the q profile is the plasma current and it was not possible to alter q while holding other relevant parameters constant.

4. Discussion and outlook

The peaking of the helium and boron density profiles has been investigated over a wide range of plasma parameters in dedicated ASDEX Upgrade discharges. The electron cyclotron resonant heating, neutral beam injection heating and the plasma fuelling were used as external actuators to modify the kinetic profile gradients and the plasma collisionality.

It is experimentally observed that no danger of helium accumulation exists in this parameter space, as the helium density profile shape follows largely that of the electron

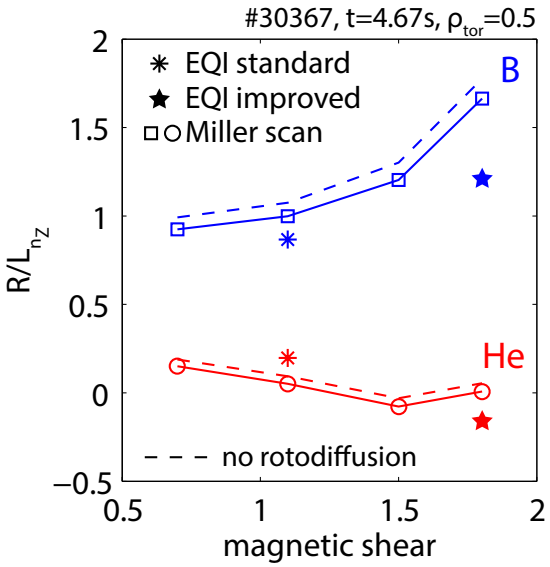

Figure 19. Variation of the predicted local normalised logarithmic impurity gradient as a function of the local magnetic shear, shown with squares for boron and circles for helium, scanned using Miller parametrisation. The predictions for the routinely available magnetic equilibrium reconstruction ("EQI standard") and for a pressure constrained equilibrium ("EQI improved") are shown with stars.

density. Generally, helium is as peaked as the electron density at high ECRH fraction, or less peaked than the electron density at high NBI fraction. The boron density profile is observed to be consistently less peaked than the electron density profile.J

Decoupling the parameters on which the impurity gradients depend is experimentally not possible, as the external actuators modify more than one plasma parameters at once. Nevertheless, this extensive, multi-species database has proven to be a valuable tool and a strict test of the modelling predictions. Detailed comparisons of the experimental local normalised logarithmic gradients of the impurity density profiles at the plasma mid-radius with the modelling predictions obtained by means of quasi-linear and a limited set of nonlinear simulations with GKW were performed. While qualitative, or even quantitative agreement can be obtained between the experiment and the prediction for subsets of the database (as shown in other studies), this does not hold for all cases. On the contrary, completely different trends can be obtained, with the discrepancies becoming larger for boron with dominant NBI heating, and the opposite for helium. Furthermore, when agreement is observed, the simulations can still not reproduce the experimental peaking of both impurities simultaneously. It can be concluded that the theoretical description of low-Z impurity transport within the quasi-linear model applied here is incomplete. Discrepancies between experiment and theory have also been identified for low-Z impurities in JET, in H-mode plasmas with the C-wall [37] (studied using GKW) and in L-mode plasmas with the ITER-like wall [6] (studied using GENE). The experimental observations of increasing discrepancies for B with dominant NBI heating and high fast-ion pressures indicate that fast ions may play an important role. This is the topic of ongoing work.

The experimental work presented here was based on steady state impurity density

gradients. From the experimental point of view, the development of methods to obtain the diffusion coefficient and the convective velocities of low-Z impurities using perturbation studies, is very valuable (see [40] for an example). As shown in Fig. 10, there are indications that the convective velocities predicted by the simulations are not correct, but it is not possible to confirm that the diffusion coefficients are correct. The separation of the two components will help to identify the missing elements in the theoretical description and guide the way for further theoretical work. In addition, multi-machine comparisons can provide valuable information in different regimes and for different impurities. Other low-Z impurities, such as nitrogen or neon can also be included for a wider scan in the impurity charge and mass.

Furthermore, direct experimental measurements of the turbulence are paramount in any turbulent transport studies. The experimentally measured turbulence levels can be compared to the gyrokinetic modelling. ASDEX Upgrade has a large suite of reflectometry diagnostics [41, 42, 43, 44], including Doppler reflectometry and poloidal correlation reflectometry, as well as correlation ECE [45], capable of delivering electron density and temperature fluctuation measurements. However, fluctuation measurements could not be provided as far in as mid-radius in the discharges of this transport database. Future work can focus on developing plasma scenarios in which all measurements can be made. However, due to the strong restrictions, such a comparison is limited to a single or a few plasma conditions. Furthermore, different diagnostic methods capable of measuring fluctuation in the plasma core need to be realised.

From the theoretical and modelling point of view, a few next steps are envisaged. Additional non-linear gyrokinetic simulations can expand on and further validate the quasilinear approach used here, as was done in [3], and allow the matching of the total fluxes to the experimental ones. However, global simulations might be needed to explain the experimentally observed peaking of the low-Z impurity density profiles. Adding "global" elements to the local description can be very useful in this direction [46]. Finally, synergies between turbulent and neoclassical transport should be considered [47].

To conclude, an extensive experimental database for studies of low-Z impurity transport was assembled which provided significant insight into the behaviour of helium and boron in ASDEX Upgrade, as well as a very valuable tool for benchmarking against impurity transport models. At present, the modelling is not able to describe the experimental observations. No direct conclusion can be drawn on which transport mechanism is responsible for the discrepancies between the experimental observations and the modelling predictions, motivating further theoretical and modelling work on this topic utilising these experimental data.

Acknowledgment

This work has been carried out within the framework of the EUROfusion Consortium and has received funding from the Euratom research and training programme 2014-2018 and 2019-2020 under grant agreement No 633053. The views and opinions expressed herein do not necessarily reflect those of the European Commission.

References

[1] D. Finkenthal, Ph.D. thesis, University of California, Berkeley, 1994.
[2] C. Angioni *et al.*, Nucl. Fusion **51**, 023006 (2011).
[3] F. J. Casson *et al.*, Nucl. Fusion **53**, 063026 (2013).
[4] C. Angioni *et al.*, Nucl. Fusion **49**, 055013 (2009).
[5] A. Kappatou *et al.*, Plasma Phys. Control. Fusion **60**, 055006 (2018).
[6] N. Bonanomi *et al.*, Nucl. Fusion **58**, 036009 (2018).
[7] R. Dux *et al.*, Nucl. Fusion **44**, 260 (2004).
[8] H. Takenaga *et al.*, Nucl. Fusion **43**, 1235 (2003).
[9] V. Rohde *et al.*, 26th EPS Conf. on Controlled Fusion and Plasma Physics **23**, 1513 (1999).
[10] E. Viezzer *et al.*, Rev. Sci. Instrum. **83**, 103501 (2012).
[11] R. Jaspers *et al.*, Rev. Sci. Instrum. **83**, 10 (2012).
[12] A. Ware, Phys. Rev. Lett. **25**, 15 (1970).
[13] C. Angioni *et al.*, Nucl. Fusion **44**, 827 (2004).
[14] R. M. McDermott *et al.*, Plasma Phys. Control. Fusion **53**, 124013 (2011).
[15] R. M. McDermott *et al.*, Plasma Phys. Control. Fusion **53**, 035007 (2011).
[16] B. Streibl *et al.*, Fusion Science and Technology **44**, 578 (2003).
[17] R. McDermott *et al.*, Plasma Phys. Control. Fusion **60**, 095007 (2018).
[18] W. Heidbrink *et al.*, Commun. Comput. Phys. **10**, 716 (2011).
[19] B. Geiger *et al.*, Plasma Phys. Control. Fusion **53**, 065010 (2011).
[20] B. Geiger, Ph.D. thesis, Ludwig-Maximilians-Universität, München, 2012.
[21] R. J. Fonck, D. S. Darrow, and K. P. Jaehnig, Phys. Rev. A **29**, 3288 (1984).
[22] R. Fischer *et al.*, Fusion Sci. Technol. **58**, 675 (2010).
[23] P. McCarthy, Phys. Plasmas **6**, 3554 (1999).
[24] R. Dux *et al.*, J. Nucl. Mater. **313**, 1150 (2003).
[25] A. G. Peeters, Phys. Plasmas **7**, 268 (2000).
[26] R. Dux and A. G. Peeters, Nucl. Fusion **40**, 1722 (2000).
[27] M. Frojdh, M. Liljestrom, and H. Nordman, Nucl. Fusion **32**, 419 (1992).
[28] C. Angioni and A. G. Peeters, Phys. Rev. Lett. **96**, 095003 (2006).
[29] Y. Camenen *et al.*, Phys. Plasmas **16**, 012503 (2009).
[30] T. Hein and C. Angioni, Phys. Plasmas **17**, 1 (2010).
[31] A. G. Peeters and D. Strintzi, Phys. Plasmas **11**, 3748 (2004).
[32] A. G. Peeters *et al.*, Comput. Phys. Commun. **180**, 2650 (2009).
[33] A. G. Peeters, C. Angioni, and D. Strintzi, Phys. Rev. Lett. **98**, 265003 (2007).
[34] F. J. Casson *et al.*, Phys. Plasmas **17**, 102305 (2010).
[35] D. Told *et al.*, Phys. Plasmas **20**, 122312 (2013).
[36] TRANSP references http://w3.pppl.gov/transp/refs, 1998.
[37] P. Manas *et al.*, Phys. Plasmas **24**, 062511 (2017).
[38] M. G. Dunne *et al.*, Nucl. Fusion **52**, 123014 (2012).
[39] R. Waltz and R. Miller, Phys. Plasmas **6**, 4265 (1999).
[40] C. Bruhn *et al.*, Plasma Phys. Control. Fusion **60**, 085011 (2018).
[41] G. D. Conway, Nucl. Fusion **46**, S665 (2006).
[42] G. D. Conway *et al.*, Proc. 9th International Reflectometry Workshop, Lisbon (2009).
[43] D. Prisiazhniuk, Ph.D. thesis, Technische Universität München, 2017.
[44] A. Silva *et al.*, Rev. Sci. Instrum. **67**, 4138 (1996).
[45] S. J. Freethy *et al.*, Phys. Plasmas **25**, 055903 (2018).
[46] D. R. Mikkelsen *et al.*, Phys. Plasmas **22**, 062301 (2015).
[47] D. Estéve *et al.*, Nucl. Fusion **58**, 036013 (2018).